Mixing Regime Simulation and Cellulose Particle Tracing in a Stacked Frame Photocatalytic Reactor

Nagarajan, S., Stella, L., Lawton, L. A., Irvine, J. T. S., & Robertson, P. K. J. (2017). Mixing Regime Simulation and Cellulose Particle Tracing in a Stacked Frame Photocatalytic Reactor. *Chemical Engineering Journal*, *313*, 301-308. https://doi.org/10.1016/j.cej.2016.12.016

Published in:
Chemical Engineering Journal

Document Version:
Peer reviewed version

Queen's University Belfast - Research Portal:
Link to publication record in Queen's University Belfast Research Portal

Mixing Regime Simulation and Cellulose Particle Tracing in a Stacked Frame Photocatalytic Reactor

Sanjay Nagarajan[a], Lorenzo Stella[a,b], Linda A. Lawton[c], John T.S. Irvine[d] and Peter K.J. Robertson[a]*

[a]Centre for the Theory and Application of Catalysis (CenTACat), School of Chemistry and Chemical Engineering, Queen's University Belfast, David Keir Building, Stranmillis Road, Belfast, BT9 5AG, United Kingdom;

[b]Atomistic Simulation Centre (ASC), School of Mathematics and Physics, Queen's University Belfast, University Road,

Belfast BT7 1NN, UK,

[c]School of Pharmacy and Life Sciences, Sir Ian Wood Building

Robert Gordon University, Garthdee Road, Aberdeen, AB10 7GJ, United Kingdom

[d]JTSI Group, University of St. Andrews, School of Chemistry, Purdie Building, North Haugh, St Andrews, KY16 9ST, United Kingdom;

*Corresponding authors, *p.robertson@qub.ac.uk Tel: +44 (0) 28 9097 4627, snagarajan01@qub.ac.uk*

Abstract

To sustainably meet the global energy demand, unconventional methods to produce renewable energy must emerge. Biofuels from cellulose (via fermentable sugar production) mediated via photocatalysis provides an alternative to conventional fossil fuels. In order to effectively drive photocatalytic processes an effective reactor design is required, the design of which is influenced by a number of key factors such as the catalyst to reactant ratio and residence time, catalyst illumination time, light penetration and distribution for the system, mass transfer limitations (mixing) and product recovery. In this study we use COMSOL Multiphysics® to simulate and assess one of the mentioned parameters – mixing regime of cellulose particles in a Stacked Frame Photocatalysis Reactor (SFPR). In the reactor design, we compare two mixers: a 'plus' shaped magnetic stirrer bar and an 8 blade Rushton impeller. The simulations reveal that the Rushton impeller offers a radial mixing pattern with a higher fluid velocity of 1.2 m/s when compared to the stirrer bar that offers a fluid velocity of 0.9 m/s. Cellulose particle tracing simulations confirm that the particle dispersion is superior in the case of the Rushton impeller as the vorticity generated during the mixing push the particles to the reactor's walls. Since the particles are forced towards the walls, there is a probability of more particles being illuminated than in the case of no or improper mixing.

Keywords: Photocatalysis, COMSOL, fermentable sugars, mixing, simulation.

1. Introduction

Fossil fuel depletion and raising greenhouse gas emissions have increased the need for alternative renewable energy technologies. Along with solar energy, wind energy and tidal energy, biofuels could also contribute to the global clean energy production. Biofuel production could be brought about from various sources such as waste vegetable oil, food waste, animal fats, algae and cellulose. Among these sources, cellulose is the most attractive raw material as it is the world's most abundant organic material [1]. However, cellulose as such cannot be used directly as a fuel and has to be converted to fermentable sugars which can then lead to the production of bio alcohols via fermentation. Conventionally, cellulose hydrolysis has been achieved through environmentally unfavourable, high energy consuming physico-chemical methods such as steam explosion, pyrolysis or acid/alkali hydrolysis [2]. A potential new route for cellulose breakdown using photocatalysis could be an alternative, more sustainable method to breakdown the cellulose molecule to smaller carbohydrate species [3]. Photocatalysis is a light driven chemical reaction. When light of a specific wavelength with energy greater than or equal to band gap energy illuminates a photocatalyst, an electron from the valence band (VB) gets promoted to the conduction band (CB) leaving behind a positive hole in the VB. These positive holes react with water or OH^- to form hydroxyl radicals which can carry out oxidation reactions such as break down of cellulose.

Conventional reactors for chemical engineering are well established and classified, whereas photocatalytic reactor designs are relatively new [4]. In addition

to the conventional reactor design parameters such as reactor geometry, mixer configuration, mode of operation (continuous or batch), separation efficiency, residence time, reaction selectivity, materials of construction and cost, the following parameters with respect to illumination needs to be considered while designing a photocatalytic reactor [5],

(i) Type of illumination source

(ii) Output power of the light source

(iii) Spectral distribution

(iv) Maintenance

(v) Inclusion of reflectors, mirrors and windows

(vi) Construction materials to facilitate light transmission

Furthermore, the illumination source also influences the choice of materials for reactor construction. When external ultraviolet (UV) light sources are used for photocatalysis, expensive fused silica (quartz) is the primary choice of material for the reactor vessel as standard glass is not t fully transparent to UV radiation, especially at wavelengths less than 400 nm. Pyrex glass, which is a cheaper alternative may, however, be used under near UV illumination (350-400 nm) or for visible light photocatalysis. When illumination sources are deployed within the reactor, the unit is made of materials such as aluminium or stainless steel (for reflection and light distribution), however Pyrex or quartz lamp housing units will still be required. A range of light sources that could be used to illuminate the TiO_2 photocatalytic system is summarised in Table 1. In addition, sample spectra of two

commonly used UV lamps (500 W Xenon lamp and 36 W fluorescent UV lamps) are shown in Figure 1.

Table 1.

Figure 1.

As previously reported in the literature, photocatalytic reactor designs can potentially fulfil the following objectives: [6-8]

(i) Improve the catalyst to reactant ratio and residence time,

(ii) Increase the catalyst illumination time,

(iii) Improve light penetration and distribution for the system,

(iv) Eliminate mass transfer limitations and

(v) Increase the product production and recovery.

Photocatalytic reactors can be broadly grouped under either suspended or immobilised photoreactors based on the mode of photocatalyst deployment. It is not feasible to compare the current reactor designs on a common scale as they have their own advantages and disadvantages based on their area of application [4]. Recently, however, 12 different photocatalytic reactors for wastewater treatment were compared using a benchmark ratio proposed as the photocatalytic space time yield (PSTY) [6]. According to Leblebici *et al.* PSTY is defined as “the volume of water treated for each kW lamp power per volume of reactor per unit of time” [6]. After normalising various designs using PSTY, they concluded that the pilot scale

slurry reactor with a suspended photocatalyst system outperformed the other designs. This was as a result of issues such as high light distribution, decreased mass transfer limitation and high photocatalyst surface area available for illumination and hence is also the most commonly used reactor design in the field of photocatalysis [9, 10].

Simulation is a useful tool to compare various reactor configurations or to compare different modifications done to the same reactor design without having to fabricate the actual unit thereby making it a useful tool in engineering design to reduce the time and costs. There are numerous software packages available for such simulations including MATLAB®, ANSYS®, COMSOL Multiphysics®, and SOLIDWORKS®. The rotating machinery turbulent flow k-ε model in COMSOL Multiphysics® 5.1 was used in this study [11]. The reason for choosing k-ε model for the simulations are as follows,

(i) This model uses minimal computational resources,
(ii) Offers a good trade-off between accuracy and the computational resource requirement,
(iii) Performs well when the pressure drop in the system is expected to be negligible,
(iv) Provides an approximation of the flow patterns for a new design, such as the SFPR.

Simulation and modelling have been reported earlier for chemical reactions, multi-phase fluid flow, mixing, filtration, dialysis and other processes, [11-16] but only

for a limited number of applications in photocatalytic reactors. Simulations focussing especially on mixing regimes in a reactor using COMSOL Multiphysics® have been performed in the past for reactor design verification and bioethanol fermentation purposes [11, 16]. Patel *et al*. performed COMSOL Multiphysics® simulations to determine the best possible mixing profiles to understand the mass transfer for a combination of either ellipsoidal or flat base vessel with five different impeller blade configurations [11]. Similarly, Rana performed simulations to determine the mixing profiles of marine impeller and Rushton impeller for bioethanol fermentation [16]. Furthermore, Rana reported that marine impellers were superior in performance and cost efficient over Rushton impellers for bioethanol fermentation in a stirred tank reactor. This paper describes the design of a novel SFPR (slurry reactor design) along with its mixing regime simulations of a commercially available 'plus shaped' stirrer bar and an 8 blade Rushton impeller configuration for the SFPR.

2. Methodology

2.1 Stacked Frame Photocatalysis Reactor (SFPR) design

A novel SFPR was designed using FreeCAD 15.0. The SFPR design consists of the following parts,

(i) Perspex frames (with and without inlet/outlet ports)

(ii) Pyrex end plates

(iii) Acrylic inlet and outlet port tubes

(iv) Silicone rubber gaskets

(v) Nylon threaded rods, nuts and washers

(vi) ‘Plus’ shaped magnetic stirrer bar or a stainless steel 316 grade impeller (8 blade Rushton impeller)

Figure 2 shows the front view of the SFPR frames displaying the dimensions, M6 slots for inserting the threaded rods and the slots for holding the reaction mixture (cellulose + water + TiO_2). The thickness of each frame is 10 mm and the liquid holding volume of each frame is 12 ml. All the silicone gaskets were of the same dimensions as the Perspex frames, except that the thickness was 1.5 mm. Similarly, the Pyrex end plates were also of the same dimensions as the Perspex frames, except that the thickness was 3.8 mm and there was no slot for the liquid holding volume.

Figure 2

Two Perspex frames were also designed to have inlet and outlet ports as shown in Figure 3. Multiple frames were stacked together with alternating gaskets and sandwiched between Pyrex end plates on either side to form the SFPR.

Figure 3

Threaded ports (Figure 4) made of acrylic tubes were further fixed to the inlet and the outlet ports of the frames to facilitate inflow and outflow of the reaction mixture. A light source would be positioned in such a way so that it faces the end plate adjacent to the frame with the inlet port.

Figure 4

To facilitate mixing in the reactor, a commercially available ‘plus shaped’ magnetic stirrer bar configuration and an 8 blade Rushton impeller was designed to fit the liquid holding volume of the SFPR (Figure 5). The dimensions of the stirrer bar are 19.1 mm × 9.5 mm × 2mm (width × height × thickness) and that of the stirrer bar are 20 mm × 15 mm (total width × total height), 4 mm × 5 mm (blade height × blade width) and a shaft diameter of 1 mm.

Figure 5

Despite the extensive use of baffles in conventional chemical reactors, no baffles were installed in this assembled photocatalytic reactor. The reasons for this being that the baffles might block the light reaching the photocatalyst, avoid vortex formation thereby diminishing chances of forcing the reaction mixture towards the walls (and the illumination source), hence creating “dead layers” and decreasing the fluid-particle mass transfer [17].

2.2 Mixing simulation

A flow chart on the simulation procedure is given in Figure 6. Firstly, the geometry of the fluid domain (liquid holding domain) of the SFPR was created in the COMSOL Multiphysics® 5.1 workspace assuming that 4 frames were stacked together. When 4 frames are stacked together, the liquid holding domain measures 40 mm × 40 mm × 30 mm (thickness × width × height) and has a volume of 48 ml.

The inlets and the outlet ports were also created. Secondly, the mixer (either the stirrer bar or the impeller) was created.

Figure 6

Once the geometry of the system was defined, rotating machinery turbulent flow k-ε model with a frozen rotor study (stationary with respect to the reactor) was selected in COMSOL Multiphysics®. This model uses incompressible fluid flow and assumes Reynolds-Averaged-Navier-Stokes (RANS) equation for the fluid flow [11]. Next, the material in the fluid domain was defined as water. Its fluid properties were defined with the density being 1000 Kg/m^3 and the dynamic viscosity being 1.002 × 10^{-3} Pa.s. Then the rotating domains were allotted and the speed of rotation of the mixer was set at 1000 rpm. Subsequently, the inlet was assigned and the normal inflow velocity of the system was set at 0.01 m/s. The outlet for the system was then defined with the backflow suppressed. Finally, flow continuity was set up for the rotating and the fluid domains. All domains were meshed using the “physics controlled mesh” option provided by COMSOL Multiphysics® model builder and hence automatic (Figure 7).

Figure 7

2.3 Particle tracing

Once mixing simulation was completed, particle tracing module was added to the model to simulate the motion of cellulose particles in the SFPR. Then a new time

dependent study was included in the model for particle tracing. A drag force node was introduced to the module where the fluid domain defined in the mixing simulation was chosen as the domain where the particles will be present. The velocity field and the dynamic viscosity from the mixing simulation results were used to compute the drag force on the cellulose particles. The inlet and the outlet for the cellulose particles were then defined. The number of particles per release was set as 3000. From the mixing simulation results, the velocity field was chosen and defined as the initial velocity of the particles for particle tracing. In the particle properties section, the density of the cellulose particles was set as 1500 kg/m^3 (an average value obtained from literature) [18] and the particle diameter was set as 55 µm (obtained as an average diameter for cellulose particle from various suppliers). Furthermore, to use the results from the mixing simulation for the velocity field and to reduce the computation time for particle tracing, in the time dependent solver settings, the mixing simulation study was selected and included. The time range to compute the motion of the cellulose particles was chosen from 0 seconds to 1 second, with a step time of 0.1 seconds to visualise the mixing at the initial stages. It has to be noted that, this SFPR was originally designed for the purpose of photocatalytic cellulose breakdown and hence cellulose particles were used as model particles to simulate particle tracing, however this reactor could also be used for other generic photocatalytic applications such as wastewater treatment.

3. Results and discussion

3.1 Mixing simulation

Mixing simulation for the SFPR with the ‘plus shaped’ stirrer bar and an 8 blade Rushton impeller configurations were performed and results in the form of slice

plots, XY streamline plots and YZ streamline plots were generated and summarised in Figure 8 and Figure 9 respectively. As seen from Figure 8, the arrows indicate the direction of fluid flow as a result of mixing where the size of the arrows is proportional to the fluid velocity at that point. It can be observed that the fluid velocity is higher (as seen from the proportional arrows) close to the blades of the Rushton impeller when compared to the walls of the stirrer bar. This observation is explained by the flat blade impeller exerting a relatively stronger force on the fluid than the convex walls of the stirrer bar. This explanation is further supported by the specific velocity magnitudes where the maximum fluid velocity close to the walls of the impeller blade and the stirrer bar is 1.2 m/s and 0.9 m/s respectively.

Figure 8

Figure 9 shows the XY and YZ streamline plots of the mixing profiles respectively in the SFPR with a plus shaped stirrer bar and the 8 blade Rushton impeller. As can be seen from the XY plot, a prominent circular flow is developed with the stirrer bar, however it is not the case with the Rushton impeller. The arrows indicate the direction of fluid flow during mixing. The velocity magnitude spread across the XY plane for the stirrer bar is in the range of 0.2-0.4 m/s and that for the impeller is in the range of 0.1-1.2 m/s as seen from the streamlines and the spatial velocity fields.

Figure 9

Furthermore, Figure 9 also shows that there are no obvious “dead layers” in both the cases, which is an indication that when particles are introduced in the

SFPR, they will stay in suspension. The maximum fluid velocity in both the cases is observed close to the walls of the impeller blades and the stirrer bar. Once the fluid is pushed away from the stirrer bar, the fluid velocity drops to 0.4 m/s along the walls of the SFPR. Whereas in the case of the impeller, a fully developed radial mixing pattern is observed. This observation is consistent with the existing literature [19-21]. The fluid velocity close to the top centre of the SFPR is small, indicating that a tiny vorticity is generated when the stirrer bar is used. This conclusion is also supported by the XY streamline plot. In the case of the impeller, a well-developed vorticity is seen in the middle thereby pushing the fluid towards the walls. In the case of a photocatalytic reactor (SFPR), when the liquid is forced towards the walls of the reactor, it will help in illuminating the reaction mixture evenly thereby fulfilling the need for light penetration.

3.2 Particle tracing simulation

Once the mixing simulation was completed, particle tracing simulations for cellulose in the SFPR were performed. The particle tracing simulations revealed that the motion of the cellulose particles in both the cases followed the fluid flow patterns initiated by the mixing. As a result of mixing, in both the cases, cellulose particles were well dispersed in the suspension. In the case of the impeller, as a result of a prominent vorticity developed due to agitation, the particles enter the vortex first along with the fluid flow and with the constant rotation of the impeller they are pulled closer to the blades and instantaneously pushed towards the walls.

TiO_2 photocatalyst particles are water insoluble white odourless transition metal oxide powders that have a bandgap of 3.2 eV which corresponds to an

excitation wavelength of 387 nm [22]. One of the most commonly used forms of TiO_2 is the Evonik P25 form which is a mixture of 70 % anatase and 30 % rutile crystal phases of TiO_2. This combination is commercially preferred to avoid photocatalytic losses due to recombination [23]. The average size of TiO_2 particles are in the range of 25 – 65 nm [24], which could aggregate to form particles in the size range of microns or could adsorb on to the cellulose surface thereby considerably increasing the combined particle size. In addition, since the motion of particles in the fluid domain are proportional to the fluid motion, these photocatalyst particles are expected to have a similar motion such as that of cellulose in the fluid domain. Since the particles are forced towards the walls, the chances of more photocatalyst particles being illuminated are higher than a system which offers no mixing. This mechanism also decreases the mass transfer limitations and will help to improve the cellulose-TiO_2 particle interaction, thereby producing desired products. The videos of the cellulose particle tracing in a SFPR with the stirrer bar and the impeller can be found in the supplements as video 1 and video 2 respectively.

From literature, the scattering and absorption coefficients of P25 could be obtained which correspond to 54208 $cm^2\ g^{-1}$ and 887 $cm^2\ g^{-1}$ at 365 nm respectively [25]. It should be noted that the scattering coefficient is multiple folds (60 times) higher than the absorption coefficient which means that the majority of the light extinction depends on scattering. This was also supported by Egerton and Tooley, who reported that when illuminated at 360 nm, TiO_2 particles of a mean size 50 nm contributed only a meagre 22% for extinction [26]. They also reported that with the increase in particle size, scattering coefficient would increase. This increase could be possible in the case of cellulose-TiO_2 mix in a SFPR. With cellulose being poor light

absorbers [27] and with the possibility of TiO_2-cellulose aggregate formation, the scattering coefficient for these particles (and aggregates) would tend to increase in the SFPR and would contribute to a uniform light distribution within the reactor. In addition, from the numbers reported in literature it is evident that minimal light absorption by TiO_2 particles occurs and therefore would have an effect on photocatalysis. Hence to avoid a negative effect of minimal absorption on photocatalysis, proper mixing has to be established as reported in this study. It should be noted that more insight on the motion of particles and radiation scattering could be revealed when particle-particle interaction and the particle-radiation interaction studies are undertaken in the future.

4. Conclusion

Mixing profiles in the SFPR with various impeller and stirrer bar configurations were determined using the rotating machinery turbulent flow k-ε model in COMSOL Multiphysics® 5.1. Simulations were performed with water present in the fluid domain. The mixers were set to be operated at 1000 rpm. The results reveal that the plus shaped stirrer bar had a circular flow with the highest average fluid flow velocity around 0.9 m/s whereas, the 8 blade Rushton impeller had a superior performance than the stirrer bar and produced a radial mixing profile in addition to having higher fluid flow velocity of 1.2 m/s.

Further to the mixing profiles, particle tracing simulations were also performed in the SFPR using cellulose as the model particle. The drag force of the cellulose particles in the particle tracing were proportional to the fluid velocity obtained from

the mixing simulations. In the cases with both the stirrer bar and the Rushton impeller, the particles were well dispersed, however the particle dispersion was superior in the case of the Rushton impeller where the vorticity generated during mixing pushed the particles towards the walls. A similar particle motion is expected with the TiO_2 P25 photocatalyst due to the mixing regime generated by the Rushton impeller, thereby facilitating better illumination of the photocatalyst.

5. Acknowledgements

This work was supported by the Engineering and Physical Sciences Research Council (Project number EP/K036769/1), Robert Gordon University's IDEAS PhD studentship and Queen's University Belfast's PhD studentship. The authors would also like to thank COMSOL Ltd for support and guidance provided through their training workshop in Belfast in October 2015 and the associated trial licence access to COMSOL Multiphysics 5.1.The authors would also like to thank Professor A Prasanna de Silva, School of Chemistry and Chemical Engineering, Queen's University Belfast, for his valuable contribution during progress meetings. Supporting data are openly available on Queen's University, Belfast Research Portal, http:// pure.qub.ac.uk/portal/en/datasets/search.html.

6. References

1. G. Thoorens, F. Krier, B. Leclercq, B. Carlin, B. Evrard, Microcrystalline cellulose, a direct compression binder in a quality by design environment—A review, Int. J. Pharm. 473 (2014) 64-72.

2. Y. Sun, J. Cheng, Hydrolysis of lignocellulosic materials for ethanol production: a review, Bioresour. Technol. 83 (2002) 1-11.

3. G. Zhang, C. Ni, X. Huang, A. Welgamage, L.A. Lawton, P.K.J. Robertson, J.T.S. Irvine, Simultaneous cellulose conversion and hydrogen production assisted by cellulose decomposition under UV-light photocatalysis, Chem. Commun. (2016).

4. C. McCullagh, N. Skillen, M. Adams, P.K.J. Robertson, Photocatalytic reactors for environmental remediation: a review, J. Chem. Technol. Biotechnol. 86 (2011) 1002-1017.

5. H.I. De Lasa, B. Serrano, M. Salaices, Photocatalytic reaction engineering, 1st Edition ed., Springer, New York, 2005.

6. M.E. Leblebici, G.D. Stefanidis, T. Van Gerven, Comparison of photocatalytic space-time yields of 12 reactor designs for wastewater treatment, Chemical Engg Process 97 (2015) 106-111.

7. V. Pareek, S. Chong, M. Tadé, A.A. Adesina, Light intensity distribution in heterogenous photocatalytic reactors, Asia-Pacific Journal of Chemical Engineering 3 (2008) 171-201.

8. M.N. Chong, B. Jin, C.W.K. Chow, C. Saint, Recent developments in photocatalytic water treatment technology: A review, Water Res. 44 (2010) 2997-3027.

9. C. McCullagh, P.K.J. Robertson, M. Adams, P.M. Pollard, A. Mohammed, Development of a slurry continuous flow reactor for photocatalytic treatment of industrial waste water, J. Photochem. Photobiol. A. 211 (2010) 42-46.

10. A.E. Cassano, O.M. Alfano, Reaction engineering of suspended solid heterogeneous photocatalytic reactors, Catalysis Today 58 (2000) 167-197.

11. P. Patel, P. Vaidya, G. Singh, An Overview of Impellers, Velocity Profile and Reactor Design, Proceedings of the 2014 COMSOL Conference (2014).

12. M. Serajuddin, K. Anand Rao, T. Sreenivas, Modelling and simulation of vacuum filtration of ore slurry: a case study on limestone-hosted Indian uranium ore, Can. Metall. Q. (2016) 1-9.

13. W. Li, J. Liu, L. He, J. Liu, S. Sun, Z. Huang, X.M. Liang, D. Gao, W. Ding, Simulation and experimental study on the effect of channeling flows on the transport of toxins in hemodialyzers, J. Membr. Sci. 501 (2016) 123-133.

14. Y. Dong, F.J. Keil, O. Korup, F. Rosowski, R. Horn, Effect of the catalyst pore structure on fixed-bed reactor performance of partial oxidation of n-butane: A simulation study, Chem. Eng. Sci 142 (2016) 299-309.

15. S. Vialle, J.L. Druhan, K. Maher, Multi-phase flow simulation of CO2 leakage through a fractured caprock in response to mitigation strategies, Int. J. Greenhouse gas control 44 (2016) 11-25.

16. H. Rana, Comparison of Industrial Agitation for Simulated Batch Reactor Vessel Mixing in Bioethanol Fermentation, Proceedings of the 2015 COMSOL Conference (2015).

17. R. Alcamo, G. Micale, F. Grisafi, A. Brucato, M. Ciofalo, Large-eddy simulation of turbulent flow in an unbaffled stirred tank driven by a Rushton turbine, Chem. Eng. Sci 60 (2005) 2303-2316.

18. C. Sun, True density of microcrystalline cellulose, J. Pharm. Sci. 94 (2005) 2132-2134.

19. T. Karuppa Raj, A. Singh, S. Tare, S. Varma, Study of fluid flow around impeller blades in Rushton turbine in a baffled vessel using computational fluid dyanmics, ARPN-JEAS 9(5) (2014) 659.

20. K. Avinash, A. Joella, C. Rubio-Atoche, X. Catherine, S.N. Le, B. Joel, V. Ranade Vivek, Flow Generated by Radial Flow Impellers: PIV Measurements and CFD Simulations, Int J Chem React Eng 2 (2004) 1542.

21. Y. Tsui, J. Chou, Y.H. Hu, Blade Angle Effects on the Flow in a Tank Agitated by the Pitched-Blade Turbine, J Fluids Eng 128(4) (2006) 774-782.

22. N. Serpone, A.V. Emeline, Semiconductor Photocatalysis - Past, Present, and Future Outlook, J. Phys. Chem. Lett. 3 (2012) 673-677.

23. Q. Xiang, J. Yu, P.K. Wong, Quantitative characterization of hydroxyl radicals produced by various photocatalysts, J. Colloid Interface Sci. 357 (2011) 163-167.

24. A.A. Gribb, J.F. Banfield, Particle size effects on transformation kinetics and phase stability in nanocrystalline TiO2, Am. Mineral. 82 (2015) 717.

25. M.I. Cabrera, O.M. Alfano, A.E. Cassano, Absorption and Scattering Coefficients of Titanium Dioxide Particulate Suspensions in Water, J. Phys. Chem. 100 (1996) 20043-20050.

26. T.A. Egerton, I.R. Tooley, UV absorption and scattering properties of inorganic-based sunscreens, Int. J. Cosmetic Sci. 34 (2012) 117-122.

27. D.N.S. Hon, Weathering and photochemistry of wood, in: D.N.S. Hon, N. Shiraishi (Eds.), Wood and Cellulosic Chemistry, Second Edition, Revised, and Expanded, Taylor & Francis, 2000, pp. 513.

28. J. Tian, X. Hu, H. Yang, Y. Zhou, H. Cui, H. Liu, High yield production of reduced TiO2 with enhanced photocatalytic activity, Appl. Surf. Sci. 360, Part B (2016) 738-743.

29. C. Raillard, V. Héquet, P. Le Cloirec, J. Legrand, Kinetic study of ketones photocatalytic oxidation in gas phase using TiO2-containing paper: effect of water vapor, J. Photochem. Photobiol. A. 163 (2004) 425-431.

30. H.M. Yadav, T.V. Kolekar, A.S. Barge, N.D. Thorat, S.D. Delekar, B.M. Kim, B.J. Kim, J.S. Kim, Enhanced visible light photocatalytic activity of Cr3+-doped anatase TiO2

nanoparticles synthesized by sol--gel method, J. Mater. Sci. : Mater. Electron. 27 (2015) 526-534.

31. G. Zuo, Z. Cheng, H. Chen, G. Li, T. Miao, Study on photocatalytic degradation of several volatile organic compounds, J. Hazard. Mater. 128 (2006) 158-163.

32. J. Zhong, J. Wang, L. Tao, M. Gong, L. Zhimin, Y. Chen, Photocatalytic degradation of gaseous benzene over TiO2/Sr2CeO4: Kinetic model and degradation mechanisms, J. Hazard. Mater. 139 (2007) 323-331.

33. S.B. Kim, H.T. Hwang, S.C. Hong, Photocatalytic degradation of volatile organic compounds at the gas–solid interface of a TiO2 photocatalyst, Chemosphere 48 (2002) 437-444.

34. H. Ourrad, F. Thevenet, V. Gaudion, V. Riffault, Limonene photocatalytic oxidation at ppb levels: Assessment of gas phase reaction intermediates and secondary organic aerosol heterogeneous formation, Applied Catalysis B: Environmental 168–169 (2015) 183-194.

35. A. Miyawaki, S. Taira, F. Shiraishi, Performance of continuous stirred-tank reactors connected in series as a photocatalytic reactor system, Chem. Eng. J. 286 (2016) 594-601.

36. O.I. Tokode, R. Prabhu, L.A. Lawton, P.K.J. Robertson, Effect of controlled periodic-based illumination on the photonic efficiency of photocatalytic degradation of methyl orange, Journal of Catalysis 290 (2012) 138-142.

37. O. Tokode, R. Prabhu, L.A. Lawton, P.K.J. Robertson, The effect of pH on the photonic efficiency of the destruction of methyl orange under controlled periodic illumination with UV-LED sources, Chem. Eng. J. 246 (2014) 337-342.

38. K. Natarajan, T.S. Natarajan, H.C. Bajaj, R.J. Tayade, Photocatalytic reactor based on UV-LED/TiO2 coated quartz tube for degradation of dyes, Chem. Eng. J. 178 (2011) 40-49.

39. J. Shie, C. Pai, Photodegradation Kinetics of Toluene in Indoor Air at Different Humidities Using UVA, UVC and UVLED Light Sources in the Presence of Silver Titanium Dioxide, Indoor Built Environ 19 (2010) 503-512.

List of Figures and Tables

Figures

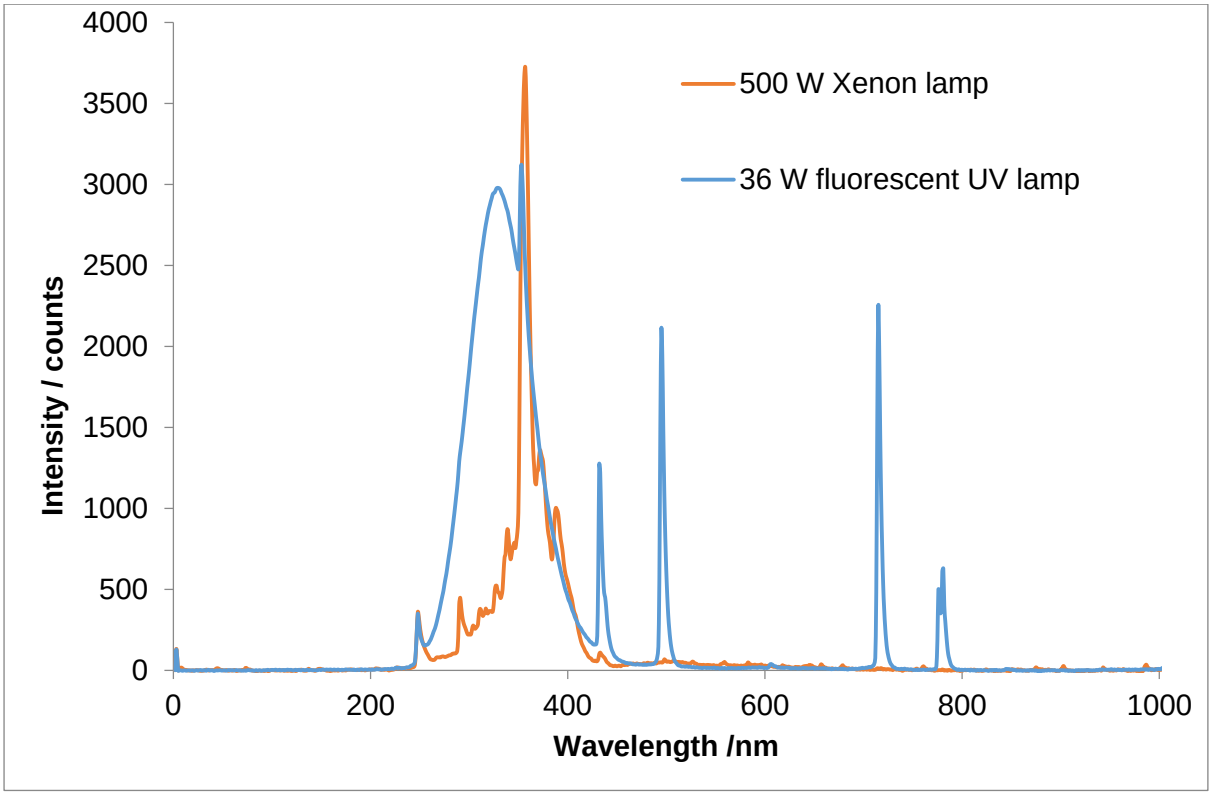

Figure 1.

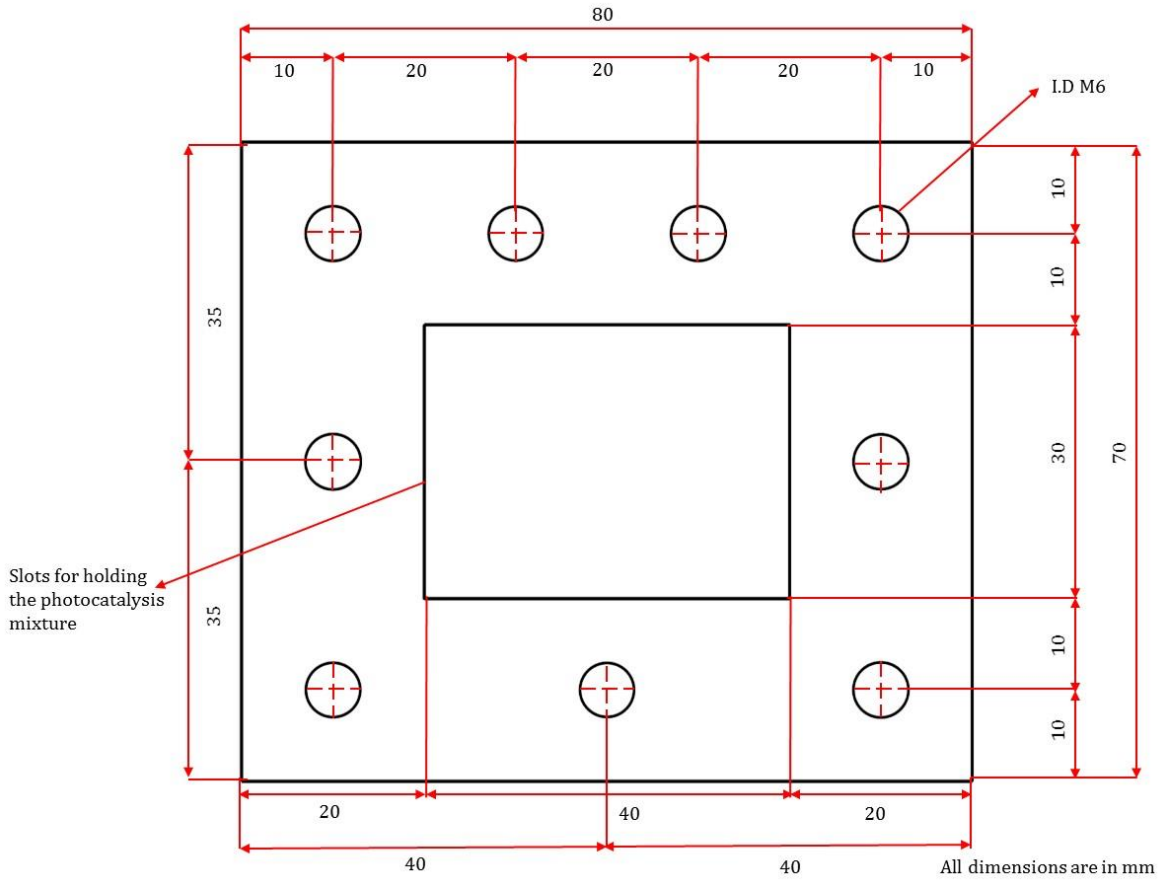
80
10
20
20
20
10
I.D M6
10
10
35
30
70
Slots for holding
the photocatalysis
mixture
35
10
10
20
40
20
40
40
All dimensions are in mm

Figure 2

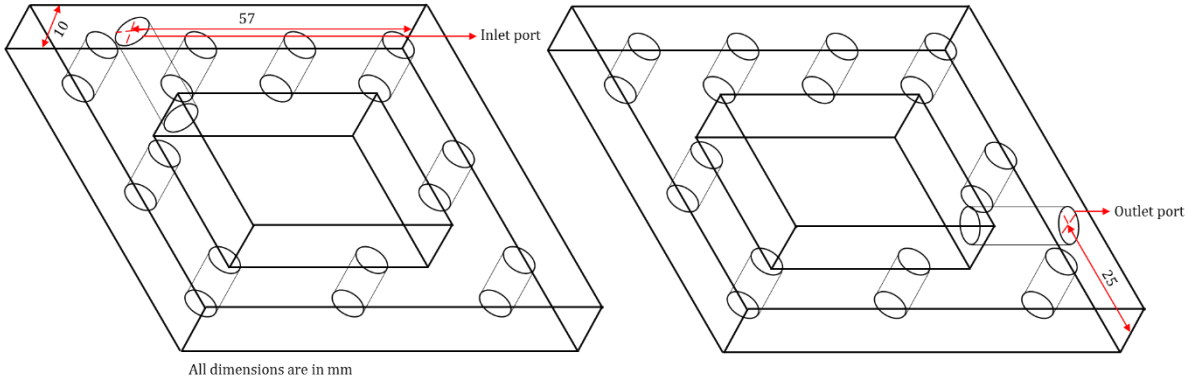

Figure 3.

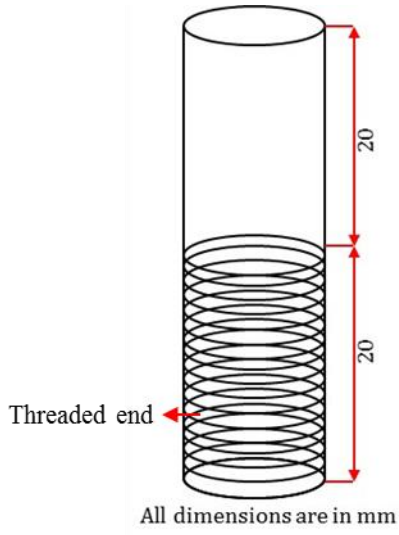

Figure 4.

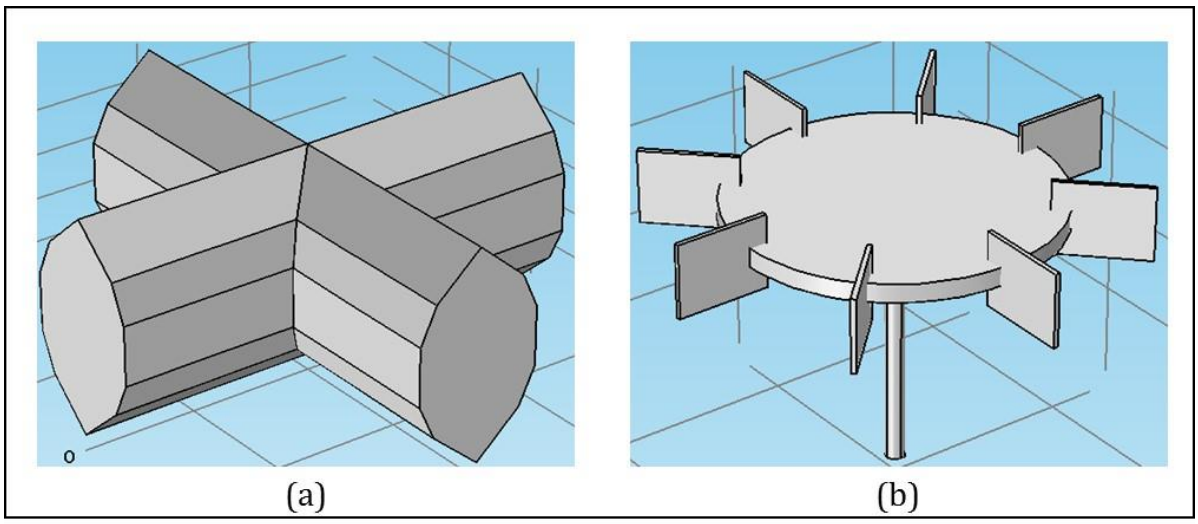

Figure 5.

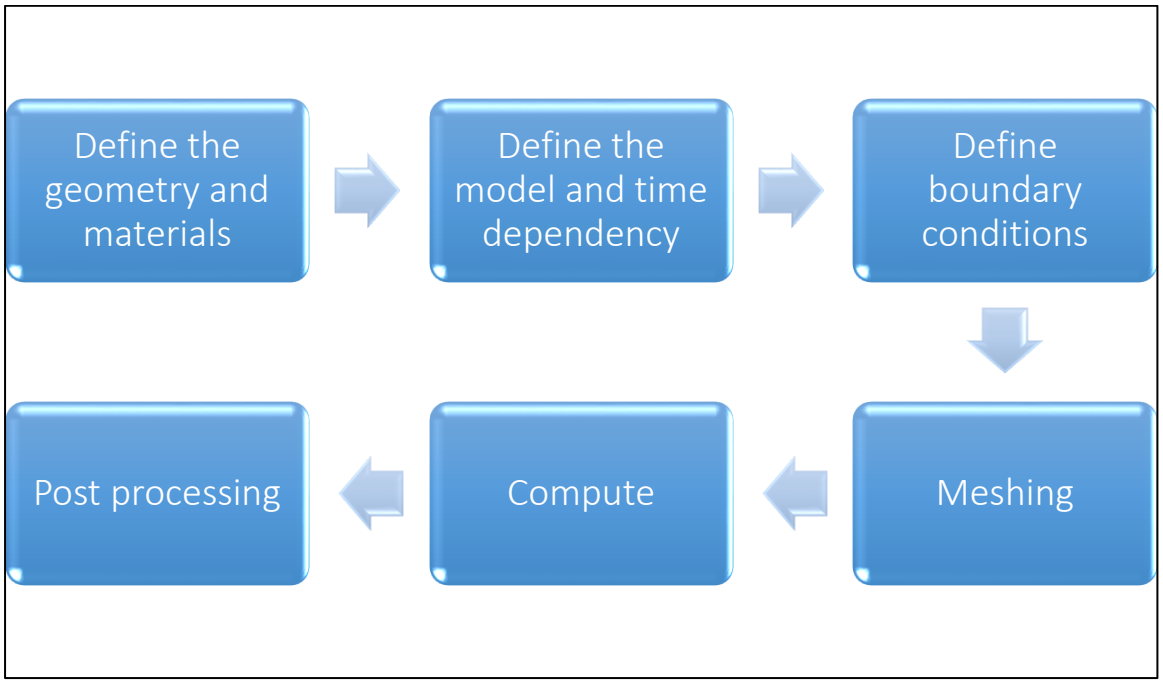

Figure 6

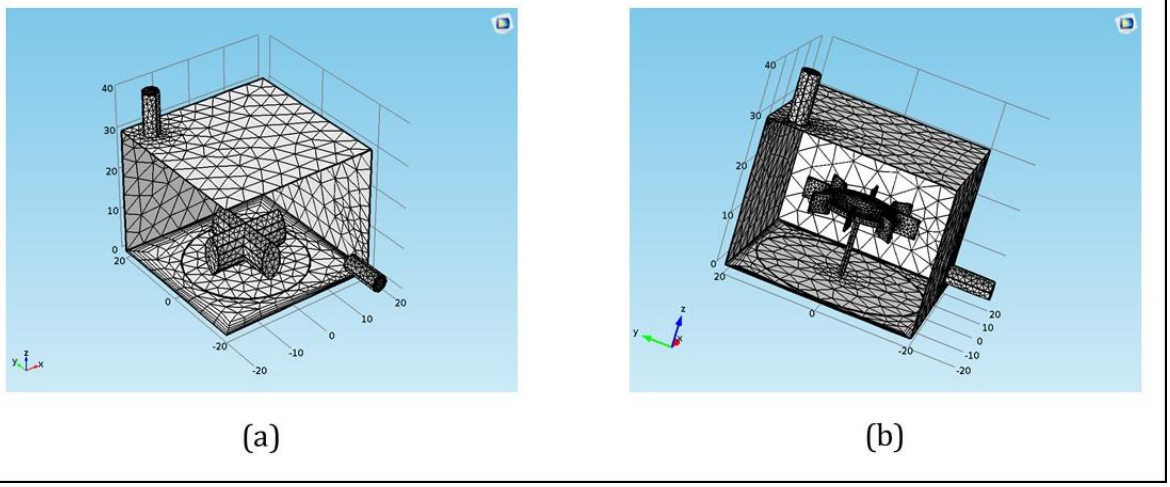

Figure 7.

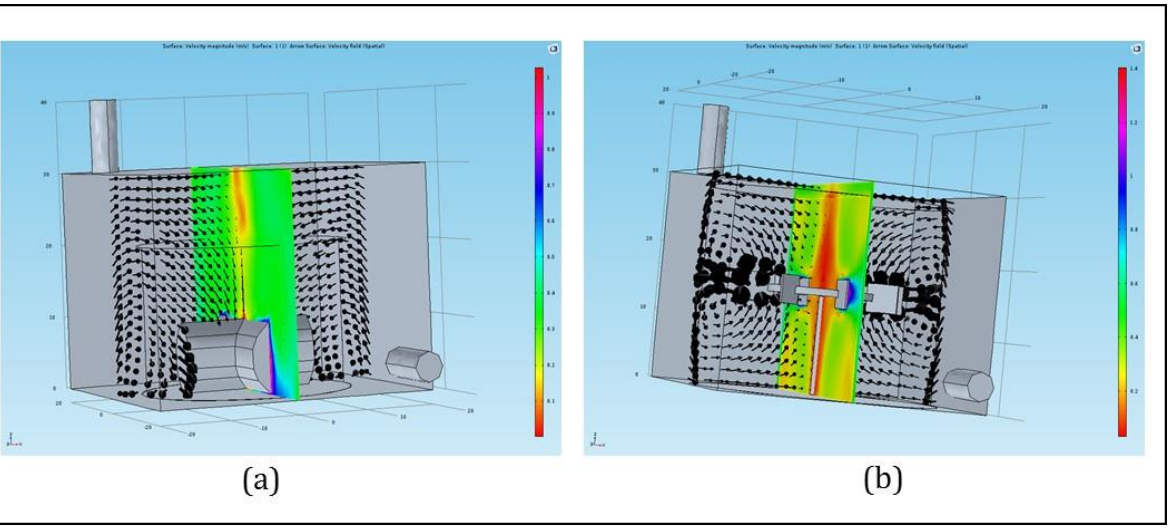

Figure 8.

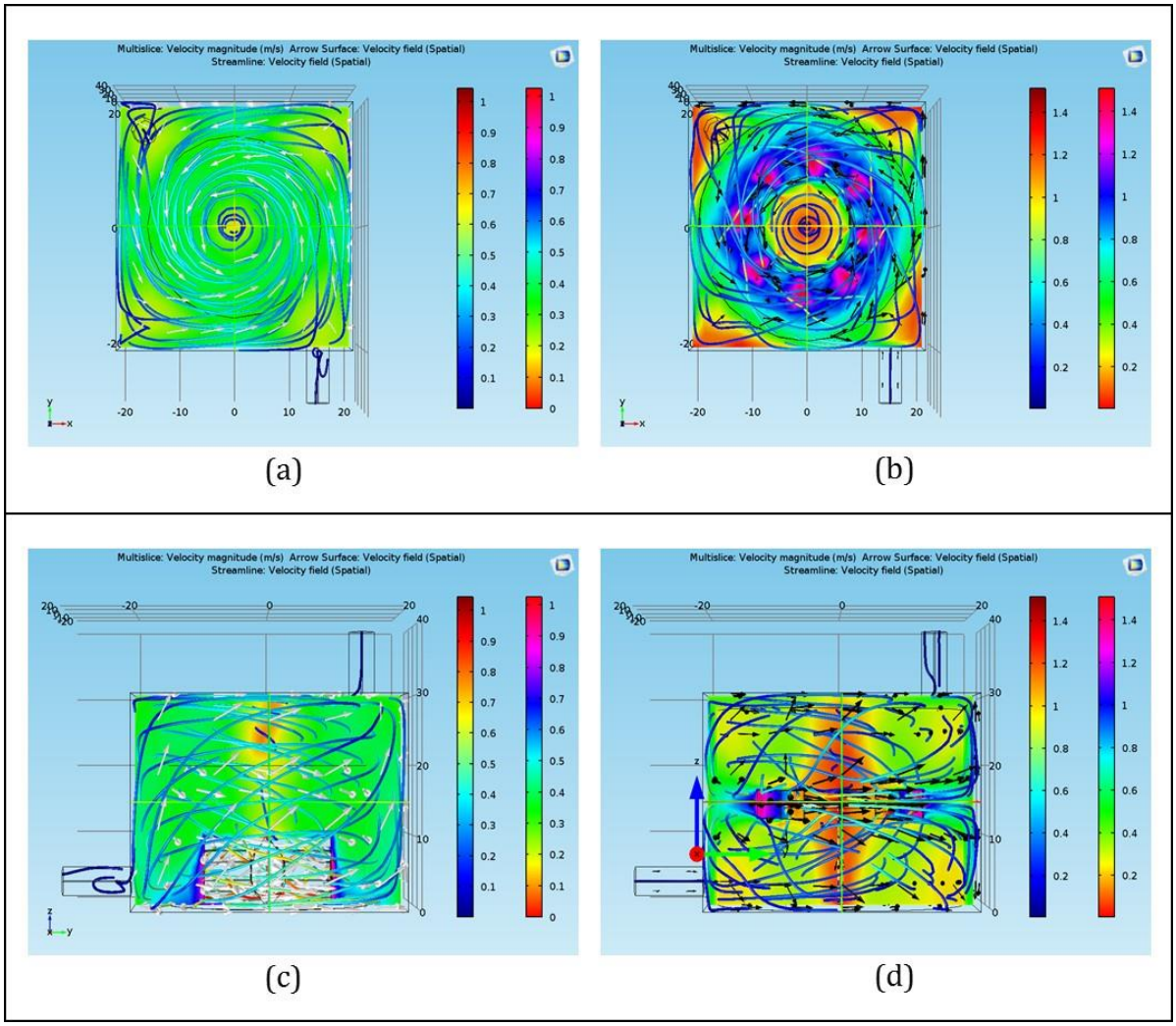
Multislice: Velocity magnitude (m/s) Arrow Surface: Velocity field (Spatial)
Streamline: Velocity field (Spatial)
(a)
(b)
(c)
(d)

Figure 9.

Type of illumination source	Spectral range	Power	Reference
Mercury arc lamp	UV and visible (265 nm – 580 nm)	300 W	[28]
Medium pressure mercury arc lamp	UV (peak at 365 nm)	700 W	[29]
Incandescent lamps	UV and visible (200 nm – 600 nm)	200 W	[30]
Mercury vapour fluorescent lamp	UV (peak at 254 nm)	6 - 10 W	[31-33]
PL-L-40 Philips UV lamps	UV (peak at 365 nm)	40 W	[34]
Blacklight blue Panasonic Fluorescent lamps	UV (300 nm – 400 nm)	4 W	[35]
Light emitting diodes (FoxUV™)	UV (peak at 360 nm)	454 µW	[36, 37]
InGaN Light emitting diodes	UV (390 nm – 410 nm)	10 – 20 mW	[38]
TG Purple Hi LED E1L5M-4P0A2-01 Light emitting diodes	UV (peak at 383 nm)	20 mW	[39]

Table 1.